Journal Pre-proofs

Bcl10 is associated with actin dynamics at the T cell immune synapse

Kaustubh Wagh, Brittany A. Wheatley, Maria K. Traver, Imran Hussain, Brian C. Schaefer, Arpita Upadhyaya

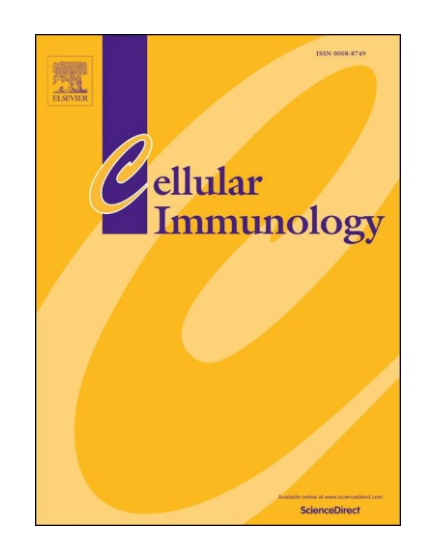
PII: S0008-8749(20)30321-X

DOI: https://doi.org/10.1016/j.cellimm.2020.104161 Reference:

YCIMM 104161

To appear in: Cellular Immunology

Received Date: 3 January 2020 Revised Date: 22 June 2020 Accepted Date: 8 July 2020



Please cite this article as: K. Wagh, B.A. Wheatley, M.K. Traver, I. Hussain, B.C. Schaefer, A. Upadhyaya, Bcl10 is associated with actin dynamics at the T cell immune synapse, *Cellular Immunology* (2020), doi: https://doi.org/10.1016/j.cellimm.2020.104161

This is a PDF file of an article that has undergone enhancements after acceptance, such as the addition of a cover page and metadata, and formatting for readability, but it is not yet the definitive version of record. This version will undergo additional copyediting, typesetting and review before it is published in its final form, but we are providing this version to give early visibility of the article. Please note that, during the production process, errors may be discovered which could affect the content, and all legal disclaimers that apply to the journal pertain.

© 2020 Elsevier Inc. All rights reserved.

Bcl10 is associated with actin dynamics at the T cell immune synapse

Kaustubh Wagh^a, Brittany A. Wheatley^b, Maria K. Traver^c, Imran Hussain^c, Brian C. Schaefer^c, Arpita Upadhyaya^{a,b*}

^a Department of Physics, University of Maryland, College Park, MD 20742, USA

^b Institute for Physical Science and Technology, University of Mary and College Park, MD 20742, USA

^c Department of Microbiology and Immunology, Uniformed Services University, Bethesda, MD 20814, USA

* Correspondence: arpitau@umd.edu

Abstract

T cell responses to antigen are intrigted by engagement of the T cell receptor (TCR)¹, leading to activation of diverse signature cascades, including an incompletely defined pathway that triggers rapid remodeling of the actin cytoskeleton. Defects in control of actin dynamics and organization are associated with several human immunodeficiency diseases, emphasizing the importance of cytoskeletal remodeling in the functioning of the adaptive immune system. Here, we investigate the role of the adaptor protein Bcl10² in the control of actin dynamics. Although Bcl10 is primarily known as a component of the pathway connecting the TCR to activation of the NF-□B

¹ TCR: T cell receptor

² Bcl10: B cell lymphoma/leukemia 10

¹ transcription factor, a few studies have implicated Bcl10 in antigen receptor-dependent control of actin polymerization and F-actin-dependent functional responses. However, the role of Bcl10 in regulation of cytoskeletal dynamics remains largely undefined. To investigate the contribution of Bcl10 in regulation of TCR-dependent cytoskeletal dynamics, we monitored actin dynamics at the immune synapse of primary murine CD8 effector T cells. Quantification of these cytamics reveals two distinct temporal phases distinguished by differences in speed and differences. Our results indicate that effector CD8 T cells lacking Bcl10 display faster actin flows and more dynamic lamellipodia, compared to wild-type cells. These studies define a role for Bcl10 in TCR-dependent actin dynamics, emphasizing that Bcl10 has impartant cytoskeleton-directed functions that are likely independent of its role in transmission CNF-□B -activating signals.

Keywords: Bcl10; T cell activation; actin dynamics; NF-□B; immune synapse; TIRF microscopy

1. Introduction

T cells are an essential component of the adaptive immune system. The T cell receptor (TCR) is stimulated by cognate profide cound to the appropriate major histocompatibility complex (MHC) allele on the surface of an antigen-presenting cell. One consequence of TCR engagement by specific antigen is activation of a downstream signaling cascade that results in rapid remodeling of the actin cybskeleton [1]. TCR interaction with stimulatory peptide-MHC results in the formation of signaling microclusters that consist of various downstream signaling molecules clustered around the cytoplasmic face of the TCR. Targets of TCR activation include the Rho family GTPases, which activate actin nucleation promoting factors (NPFs) such as WAVE2, HS1,

¹ NF-□B: Nuclear factor kappa-light-chain-enhancer of activated B cells

and WASP [1-4]. These NPFs in turn activate the Arp2/3 complex, nucleating actin polymerization, leading to large scale rearrangements of the actin cytoskeleton and force generation upon T cell activation [5–8]. The actin cytoskeleton and myosin motors subsequently assemble into a characteristic annular structure [9–11], which is a defining feature of the activated T cell immune synapse [12,13]. This remodeling of the actin cytoskeleton is a ballmark of the T cell response, leading to the formation of the immunological synapse. Dynamic remodeling of the actin cytoskeleton is a tightly regulated and biologically important process. Indeed, efects in actin remodeling are mechanistically involved in several immunodeficienci suc as Wiskott-Aldrich syndrome (WAS) [6]. Defining the molecular mechanisms the late actin organization and dynamics at the immune synapse following TCR activate therefore, of fundamental importance. Notably, the mechanisms linking the active on of TCR-initiated signaling pathways y understood. to changes in cytoskeletal dynamics remain

B cell lymphoma/leukemia 10 (Bcl10) is small, ubiquitously expressed adaptor protein consisting of an N-terminal caspase recruitment domain (CARD) and a C-terminal region with no identified consensus functional domains or artifis. A large number of T cell studies collectively implicate Bcl10 as a key constituent of a TCR-dependent cytoplasmic NF-\(\Pi\)B signaling intermediate, referred to as the caspase recruitment domain family member 11 (Card11)-Bcl10-mucosaassociate Llynphoid tissue lymphoma translocation gene-1 (Malt1) (CBM) complex [14–16]. A the absoluce of Bcl10 expression, the CBM complex cannot form, and TCR-induced NF-\(\Pi\)B activation is highly impaired. Consequences include defects in production of the critical T cell autocrine growth factor, interleukin-2 (IL-2), and several additional activation-associated proteins. Bcl10-\(^1\)-T cells exhibit poor proliferative responses and defective effector differentiation [17,18]. Defects in CBM complex signaling are also mechanistically associated with a growing list of

primary immunodeficiencies [19], further emphasizing the importance of Bcl10 and its partners in normal immune system function.

Interestingly, a few studies have implicated Bcl10 in regulation of the actin cytoskeleton. In one such study, Rueda et al. [20] showed that, independent of its role in NF-□B activation, Bcl10 regulates actin organization in Jurkat cells and CD4⁺ primary murine T cells. identified Ser138 as a critical phosphorylation site that affects F-actin organ ut does not impact NF-\(\Pi\)B activation. However, these studies primarily employed by methods, static imaging and functional assays, leaving the role of Bcl10 in regulation toskeletal dynamics largely unaddressed. Moreover, these studies did not addless the potential role of Bc110 in regulation of the actin cytoskeleton in CD8 effector T cells calso alled cytotoxic T lymphocytes (CTLs)), a subset required for the killing of host a afec ed with intracellular pathogens. In this g cell morphology and actin dynamics in primary work, we define the role of Bcl10 in regulati murine CD8 effector T cells. We used in reference reflection microscopy (IRM) to image cell morphology and total internal reflection fluorescence (TIRF) microscopy to examine actin patial resolution in CD8 T cells. Quantification of these dynamics with high temporal nd dynamics using spatiotemporal image correlation spectroscopy (STICS) reveals two distinct temporal phases. Actin lows are fast and directed inward but rapidly slowing down during the early pha by a slower phase with steady speeds and more randomly oriented flows. alyses indicate that cells lacking Bc110 display more prominent edge dynamics Our d to wildtype cells. Our results also demonstrate that lack of Bcl10 leads to faster actin flow speeds at the T cell immune synapse during both temporal phases.

2. Results

2.1. CD8 effector T cells lacking Bcl10 have more dynamic lamellipodia, but normal spreading kinetics

In order to probe the role of Bcl10 in the dynamics and organization of the actin cytoskeleton in primary murine CD8 effector T cells, we purified CD8 T cells from lymph nodes of wild type (WT) and Bcl10^{-/-} mice [17], followed by in vitro differentiating approximately seven days of expansion in media supplemented with interleukin-2 e confirmed by Western Blot that Bcl10^{-/-} CD8 T cells do not express Bcl10 but a express its signaling partner Malt1 at the same level as wildtype cells (Supplementary Fig. re 1). We have previously shown that Bcl10^{-/-} CD8 T cells expand and differentia efficiently when provided with ample antiTCR/anti-CD28 stimulation and interleuki -2 To investigate the dynamics of cell morphology and the actin cytoskeletoric por timulation of these CD8 effectors, we activated WT and Bcl10^{-/-} cells on an anti-TCR coated substrate. We then imaged the cells as they responded effection microscopy (IRM) [21]. Figure 1a shows a montage to TCR activation using interference of time-lapse images from a representative WT (top panel) and Bcl10^{-/-} (bottom panel) cell. From e in vies, we quantified the spreading kinetics of WT and Bcl10^{-/-} cells. The the IRM time-lap mented to obtain binary masks in order to quantify the change in the contact IRM images see Methods). We then fit the spreading area versus time curve to a hyperbolic tangent (1 nh) function to extract a spreading rate, as shown for four representative WT (black) and Bcl10^{-/-} (red) cells (Figure 1b). The spreading curves of all WT cells (N = 34) and Bcl10^{-/-} cells (N = 35 cells) followed this characteristic pattern and were fit with the *tanh* function to obtain a spreading rate for each cell, similar to our previous results on Jurkat T cells [21]. Comparison of the population spreading rates showed that Bcl10^{-/-} cells exhibited higher variability compared to WT cells even though the mean spreading rates were not significantly different (Figure 1c).

After the initial spreading phase and upon reaching their maximal spread state, cells continue to display significant protrusions and retractions of the cell edge. These morphological dynamics may be indicative of the stability of the immune synapse. From the IRM images (extracted the contours and quantified the dynamics of the edges using a le gorithm to calculate the edge velocities [9,22]. A representative snapshot of each cell own in Figure 1d. The contours are color coded such that blue contours represent ear es and red contours represent late times, while the heatmaps of the edge velocities is present protrusions (red) and retractions (blue) (Figure 1e). The WT cells show large disregard protrusion-retraction patterns while the Bcl10^{-/-} cells show sustained cycl potrusions and retractions along the cell periphery that are evident from the ipes in the heatmaps of edge velocities (2) representative cells are shown for each constition in Figure 1e). In order to quantify the dynamics of the cell boundary motion, we used a spatiotemporal spectral decomposition method [23]. This method decomposes the protru for retraction cycles along the cell edge into a small set of alled "modes", using an empirical mode decomposition and the component waveform HilbertHuang transform (HHT). We restricted our decomposition to a total of five modes to ensure e in the calculation of the modes. We also focused our analysis on the later numerica ing (past the 4 min time point), when the cells were fully extended and clear phase /retraction dynamics could be observed. We found that the low order modes were broadly distributed in frequency, representing the stochastic dynamics of the cell edge, whereas the higher order modes represented very low frequency cell-wide movements (Supplementary Fig. 2). However, Modes 2 and 3 effectively captured the protrusion-retraction dynamics of the cell

edge observed in Figure 1e. The amplitude distributions of these modes across WT and Bcl10^{-/-} cells as determined by the HHT differed slightly but significantly, with Bcl10^{-/-} cells exhibiting overall higher amplitudes, indicative of increased oscillatory dynamics of the cell edge, relative to WT (Figure 1f, g). Thus, we find that Bcl10^{-/-} cells display greater variability in their spreading kinetics as well as more dynamic edges during spreading. Since the TCR indicated spreading is actin mediated, we conjectured that these differences may be related to actin organization and dynamics at the T cell immune synapse.

2.2. WT and Bcl10-/- CD8 effector T cells display a highly dynamic actin cytoskeleton

We next examined whether the organization and dynamics of the again ring was altered in Bc110/cells. In order to study the dynamics of actin flows at the immune synapse, WT and Bcl10^{-/-} cells ing F-tractin-EGFP, a reporter that binds were transduced using a retroviral construct expre specifically to F-actin [24]. We activa ed there cells as described above, using substrate bound anti-TCR, and we monitored the actin dynamics at the synapse using Total Internal Reflection Sime lapse TIRF imaging showed dramatic actin reorganization Fluorescence (TIRF) microsco d Bcl10^{-/-} cells, upon activation by contact with the activating at the contact zone. For b surface, the actin doske ton organized itself into dynamic patterns spreading outwards in multiple 'front' or vaves' (Movie 1), which may be similar to the actin-membrane waves that with the formation of signaling clusters, as described in earlier work [9,25]. We also correlate observed a characteristic clearance of actin in the cell center (i.e. formation of an actin ring), which persisted for 1-2 minutes, followed by a recovery of actin over the entire contact zone and a closure of this ring (as shown for both WT and Bcl10^{-/-} cells in Figure 2a). This actin clearance is concurrent with the secretion of granules by CTLs, as described before [26]. The later stages of spreading were characterized by dynamic actin foci and a network of filaments in the contact zone

(Movie 1), which have been described previously for activated CD4 and Jurkat T cells [27–29]. We found that Bcl10^{-/-} cells also displayed a qualitatively similar behavior of actin clearance followed by recovery (Figure 2a). The times required for actin recovery in these cells were largely similar, $152s \pm 111s$ seconds for WT (N= 9 cells) and $128s \pm 58s$ for Bcl10^{-/-} (N = 16 cells).

The formation and closure of the actin ring and the morphological changes gests extensive lamellipodial actin dynamics during T cell activation which we have zed may be modulated by Bcl10 signaling. In order to further characterize these dynamic btained TIRF images of F-tractin-EGFP labeled actin in these cells (Figure 2b) with aporal resolution (1s time interval between frames). To quantify actin flows, we use a Special image Correlation Spectroscopy (STICS) [30], which is a technique that incorporates fluorescence intensity correlations across spatial and temporal interrogation windows in order to quantify changes in protein dynamics over time and space. tive example from STICS analysis is shown in usti Figure 2c. The resulting velocity vectors of their magnitudes (lengths of the arrows in Figure 2c) and their Airections (Figure 2c inset), both of which show temporal me dependence, we decomposed the velocity vectors resulting evolution. To better study their from the STICS analysis into heat maps of speeds or magnitudes (Figure 2d) and directional ctors as described in methods (Figure 2e). Higher speeds correspond to coherence of velocity vellows w peeds correspond to blues in the representative speed heat map (Figure 2d). Ouali e observe an initial (early) phase of higher speeds distributed peripherally (yellows panel of Figure 2d), while the later stages show a decrease in flow speeds (more blues in the heat map). From the directional coherence heat maps, we see an early stage of distinct inward directed peripheral flows (preponderance of yellows in Figure 2e, leftmost panel). Thus, both WT and Bc110^{-/-}CD8 T cells display a highly dynamic actin cytoskeleton, with both genotypes showing

the characteristic clearance and recovery of actin from the contact zone. STICS analysis on WT cells indicates the presence of two qualitatively different temporal phases in actin dynamics.

2.3. Spatiotemporal image correlation spectroscopy (STICS) reveals the existence of novel temporal behavior of actin dynamics in CD8 effector T cells

In order to compare the actin dynamics between WT and Bcl10^{-/-} cohort ought to first quantify the temporal behavior of actin flows in WT cells. Figure 3a sh temporal evolution of the probability density function (PDF) of actin flow speeds of r time, with blues indicating early times, and yellows indicating later times. We observe the t the istribution narrows and shifts leftward over time, indicating that the speeds are slower and more is htly distributed at later times. To quantify the temporal evolution of the PDF we d the system in the phase space of the ow speeds. Figure 3b shows a scatterplot of mean mean and standard deviation of the PI speed (x-axis) and the standard diviation (y-xis) of the PDF's. The scatterplot is color coded so le sllows indicate later times. As anticipated, the temporal that blues indicate early time almost monotonic decrease in both the mean and standard evolution of the system deviation of the PDF until t gets trapped in the lower left region of the phase space (Figure 3b). We then used a k-means clustering approach [31] to classify the scatterplot into two distinct igure 3c). A k-means classification can classify any set of datapoints into an arbitrary clusters number clusters. We choose to classify the data into two clusters because we qualitatively observed that the actin dynamics show two distinct types of behavior (Figure 2d, 2e). Figure 3d shows a plot of the mean actin flow speed over time for the same representative cell as in Figures 3a-c. The shaded error bars indicate 2.576*SEM, which (for a normally distributed dataset, this would correspond to the 99% confidence interval; in this case, it serves as a measure of the spread

in the data), and the colors correspond to the state assignment obtained from the k-means clustering shown in Figure 3c. We find that these state assignments correspond to two distinct phases: Phase 1 (blue) consists of higher but rapidly decreasing speeds, and Phase 2 (red) consists of slower but more stable speeds (Figure 3d).

For the rest of the analysis, we divided all the flows into these two phases, which mined separately for each cell by the same unbiased clustering approach. From the same tribution of the directional flow vectors, we defined a metric called the second se ent (SSM) to quantify the spatial distribution of inward flows. A higher SSM a more peripheral distribution of inward flows, while a lower SSM indicates ei ner intere centrally clustered or a more randomized distribution (see Methods). The two phases defined using the mean flow speed also shows a natural division for the SSM: union in the mean flow speed coincides with a reduction in the SSM. We found A decreases in the early stages during Phase 1 and becomes roughly constant at later time in Phase 2 (Figure 3e). This lower SSM at late stages is indicative of a more random distribution of flow directions concurrent with an overall decrease in the flow speeds. These observed tions indicate that actin forms a ring of fast, centripetal flows at disorganized, and disintegrate into more incoherent flows at later times. early times, which beco the speeds and directions for the entire population of cells studied, we In order to compa dative distribution function (CDF) of the flow speeds from all the velocity construc ells, after binning the data into the two temporal phases as defined above. As The CDF for the actin flow speeds is shifted to the right for Phase 1 as compared to that for Phase 2 (Figure 3f). This rightward shift indicates that, at the population level, the distribution of flows is faster in Phase 1 than in Phase 2. We also constructed the probability density function (PDF) for the directional coherence (Figure 3g). The directional coherence in Phase 1 (blue curve) shows a larger proportion of inward flows (defined as directional coherence larger than 0.8) than that for Phase 2 (orange curve), as shown in Figure 3g (inset). This observation indicates that actin retrograde flows are enhanced more in the early spreading phase than in the later phase. We similarly compared the SSM of inward flow of each phase and found that the flow in Phase 1 is higher than in Phase 2 indicating more peripheral flows in Phase 1, and more randomly oriented flows in Phase 2 (Figure 3h). These data, together with the PDF of directional concern implies that not only is there a higher proportion of inward flow in Phase 1, but als that e distribution of these flows is more peripheral in Phase 1 than in Phase 2. This ling is consistent with our observation of a band of retrograde flow in the lamellip nd lamellar regions. This phenomenon has also been described in the context of Jurka ells spreading on stimulatory planar lipid bilayers [32], suggesting that this dynamic behavior may be a general feature of actin flows in TCR-stimulated T cells.

2.4. Bcl10 modulates actin dynamics in CV8 effector T cells

We next examined actin flows in Be 10^{-/-} CD8 effector T cells and compared these to our results using WT cells. Figure 4a shows a representative montage of time-lapse images of spreading F-tractin-EGFP-expressing 2cl10 T cells. As with WT cells, we used STICS analysis to obtain flow speeds and directional coherence values as shown in the spatial heat maps (Figure 4b, c). The actin flow speeds no Be 15^{-/-} T cells also exhibit two phases with a faster initial phase and slower late phase, is observed with WT cells. We then applied our classification scheme to compare the actin dynamics in WT and Bc110^{-/-} cells. We found that the actin flows were significantly faster for the Bc110^{-/-} cells as compared to those in WT cells in both phases of activation (Figure 4d). Similar to WT cells, the directional coherence in Phase 1 for Bc110^{-/-} (blue dashed curve) shows a larger proportion of inward flows (directional coherence larger than 0.8) than that for Phase 2 (orange

curve), as shown in Figure 4e. The directional coherence values were not significantly different between Bcl10^{-/-} and WT cells in either temporal phase. We then compared the SSM of inward flow in each phase for WT and Bcl10^{-/-} cells and found that it was lower in Phase 2 than in Phase 1 for each cell type (Figure 4f). Interestingly, the SSM showed a significant difference between Bcl10 and WT cells for each phase, however the spread in the data is qui these differences are not as robust as the differences in speed. The cumulative distribution functions for the SSM for each cell type in Phase 1 (Figure 4g) and Phase 2 (Figure lustrate these differences in the SSM. We speculate that these differences in the ial structure of retrograde by ty of the immune synapse. flow are important for T cell activation, and for maintaining Our results show that similar to WT cells, Bcl10^{-/-} cells show that inward directed actin flows in the early phase, and slower randomly directed flow in challeter phase of activation. Importantly, ws during both early and late phases of cell lack of Bcl10 expression leads to faster activation, as compared to WT cells. s result indicates that Bcl10 may be important in regulating actin assembly and dynamics to maintain optimum actin flows at the immune synapse.

3. Discussion

In this study, we have used a variety of live cell imaging approaches to define novel connections between the adaptor molecule Bcl10, and TCR-dependent regulation of actin cytoskeletal dynamics in CD8 effector T cells. Interestingly, although both WT and Bcl10^{-/-} T cells formed actin rings in a similar manner, the distribution of spreading rates in Bcl10^{-/-} CD8 T cells was significantly different from that for WT cells. Also, the two cell types exhibited distinct

protrusion-retraction dynamics at the periphery of the zone of contact with the TCR-stimulating substrate. To determine whether these morphological differences were correlated with differences in cytoskeletal dynamics between WT and Bcl10^{-/-} CD8 effector T cells, we used spatiotemporal image correlation spectroscopy (STICS) analysis to measure actin flows at the cell-substrate boundary during TCR activation. Through this methodology, we initially defined distinct phases of actin flows in WT CD8 effector T cells. The first phase occurs during apply ximately the first two to three minutes of spreading, during which actin flow speeds are rapidly d ecreasing with actin flows being preferentially oriented toward the center. Imped tely ollowing this early phase, there is a distinct second phase, characterized by a red and relatively constant actin flow speeds, with more randomly oriented actin flows. We the mpared the behavior of WT and Bcl10^{-/-} T cells, which revealed that actin flow becasere substantially accelerated in Bcl10^{-/-} coherence is indistinguishable from WT cells. T cells during both phases, whereas the ona Taken together, our data show that while the absence of Bcl10 has a significant impact on a subset of parameters of TCR-dependent ackin dynamics, other parameters are not impacted, relative to the behavior of WT cells elective defects thus suggest that Bcl10 is mechanistically process or pathway that regulates specific aspects of actin dynamics, involved in the control of rather than being a signal transducer that lies upstream of all TCR-dependent signaling to the actin cytoskele secifically, our data are consistent with Bcl10 controlling an actin remodeling termines flow rates, without having a clear impact on F-actin distribution and proce directi d coherence.

We note that our observation of two temporal phases of actin dynamics in primary T cells is unique compared to prior work which described two spatial components of actin flows corresponding to distance from the cell periphery in Jurkat T cells [10]. Our qualitative observation of a distinct

band of inward directed faster flows in the early phase of spreading suggests an underlying spatial organization worth exploring. The difference in actin dynamics in these different phases may have a significant effect on signaling and cytolytic function through the development of forces across engaged TCR/ligand clusters as well as integrins. In related recent work, we have shown that actin dynamics directly modulate B cell receptor mobility and signaling [33], raising the po T cell receptor signaling may also be regulated by dynamic actin networks finding of differential actin flows over time indicates the need for future studies of til e evolution of actin dynamics and their effect on signaling (e.g. microcluster formation) nd effector function (e.g. TIRF do not have sufficient regulation of granule secretion in CD8 cells). Our current studi spatial resolution to visualize the formin-nucleated actomy cs that have been described (at ad primary T cells [11]. While it is likely previously with super-resolution imaging in both Jur that Bcl10 also modulates the dynamics future work with super-resolution imaging of myosin and actin will enable us to comynamics across spatial regions and examine the role of Bcl10 on myosin, formin, and these distinct actin architectures. Previous studies have published data showing that upon TCR enga pent, Bcl10 is recruited to the immune synapse along with its signaling partner Card 1 [34, 5. Simultaneous imaging of Bc110 and actin and actin-regulatory proteins would be in mative to further probe direct interactions between the two proteins.

To our knowledge only two previous studies have investigated connections between Bcl10 and antigen receptor-dependent actin remodeling. In the earliest publication to address this topic, Ruedaet 1. [20] showed that Bcl10 deficiency in Jurkat T cells (by shRNA silencing) and primary murine naïve T cells (by germline gene inactivation) have a reduced F-actin content in response to stimulation with soluble anti-CD3. Additional experiments with Bcl10-silenced Jurkat T cells showed that spreading on a glass substrate in response to immobilized anti-CD3 and conjugate

formation in response to SEE-presenting Raji cells were deficient. However, their studies were done with fixed cells and population assays, with significant effects observed at a single time point in each type of experiment. Notably, we found that Bcl10^{-/-} CD8 effector T cells do not display a strong defect in cell spreading, in contrast to the spreading defect reported by Rueda et al. However, primary effector T cells were not examined in that publication and neither raive T cells nor Jurkat T cells were examined in our work. Due to the above differences in study design, it is therefore difficult to directly compare the results of Rueda et al. with our findings regarding TCRstimulated F-actin dynamics.

In a later study, Marion et al. [36] investigated the role of 3ch in actin polymerization and membrane remodeling downstream of stimulation of a distinct a rigen receptor, the Fcy receptor (FcγR). Their data showed that Bcl10 deficient m cr phages have a defect in FcγR-dependent phagocytosis, due to the formation of actin-riv gocytic cups that fail to fully extend and close. pl Furthermore, these defective phagocyti cups had increased N-WASP, Arp3 and Cdc42 accumulation. Based on these observations and additional data, the authors concluded that Bcl10 dlamg actin assembly via a Rac-mediated pathway, which may be important in downcytic up closure to proceed to completion. Our data demonstrating ultimately allows phase in actin dynamics in the absence of Bcl10 are roughly consistent with the TCRdependent increase results rep Marion et al. However, whether Bcl10 regulates a similar or identical athway downstream of TCR stimulation remains an open question that will need Racde to be specifically addressed by future investigations.

Due to the paucity of data, many questions remain regarding the mechanisms by which Bcl10 is connected to regulation of actin dynamics. Firstly, it remains unclear whether signaling through the CBM complex is involved, as the RNA silencing studies of Rueda et al. [20] suggest that

neither Card11 nor Malt1 are required for TCR-dependent F-actin remodeling in Jurkat T cells. These authors identified TCR-dependent phosphorylation of Bcl10 on Ser138 as critical for this activity, and with phosphorylation of Ser138 also being insensitive to Card11 silencing. Thus, the implications of these findings are that Ser138 phosphorylation of Bcl10 is TCR-dependent but Card11 independent. Interestingly, Marion et al [36] demonstrated that blocking phorplation of Bcl10 at this site via Ser138Ala mutation results in greatly enhanced binding to Cardo (which performs a role functionally similar to Card 11 downstream of FcyR in myeloi cells Collectively, 110 from CBM complex these data suggest that phosphorylation of Ser138 may redirect B signaling to regulation of actin cytoskeletal dynamics. As su trength of TCR activation may determine the amount of Bcl10 available for signaling to **□** B as a constituent of the CBM complex vs. control of actin cytoskeleton dynamics ia mechanism that requires

"free" Bcl10. However, such a model world equive substantial additional work to validate. Although we did not investigate CTK function in this study, it is reasonable to postulate that Bcl10dependent regulation of actin dynamics may influence the efficiency of CTL lysis of target cells. Specifically, Tamzalit et al. [33], recently reported that WASP and Arp2/3 regulate the dynamic formation of actin ich produsions in the immunological synapse, which are required for efficient target cell buling. These findings are reminiscent of the above described phagocytic cup data of

Marion et al. In the macrophage system, in which a clear Bcl10-dependency was identified. Additionally, given the observations of Rueda et al, showing an impact of Bcl10 on TCR dependent conjugate formation combined with our data showing Bcl10-dependency in regulation of the rate of TCR-stimulated actin flows, CTL interactions with target cells may be altered in the absence of Bcl10. Thus, investigation of the relationship between Bcl10 expression, actin dynamics, and CTL engagement with and killing of targets is an important area for investigation.

4. Methods

4.1. Cells and reagents

Lymph nodes (LN) and spleens (SPL) were harvested from age-matched 7 - 12 week old C57BL/6J (WT) mice or Bc110-/- mice [17] (extensively backcrossed onto a C57BL/6J background). CD8 T cells were purified from suspensions of mixed LN and Dynabeads negative selection kit (Invitrogen), followed by differentiation to effector T cells via 48 hr stimulation with plate-bound anti-TCR and anti-CD28 in nedia, followed by culture in IL-2 supplemented media, as described [38,39]. All ani edures were performed e with the National Research in the USU specific pathogen free animal facility in accordan Council's Guide for the Care and Use of Laboratory Anima's (The National Academies Press). All animal experiments were approved by the Uniform Services University (USU) Institutional Animal Care and Use Committee (IAC) nit number A3448-01), under protocols MIC-15575 and MIC-18-575.

gift pEGFP-C1 F-tractin-EGFP from Dyche Mullins (Addgene plasmid [24]. The F-tractin-EGFP gene fusion was subcloned from #58473; http://n2t.net/addgene: iral vector, pSQZ, consisting of a self-inactivating MSCV backbone, an this plasmid into the pero internal promoter, which is an Epstein-Barr virus (EBV) constitutive promoter of modest electable marker encoding resistance to Zeocin. pSQZ-F-tractin-EGFP was strength ith the pCL-Eco packaging plasmid [41] into HEK293T cells to produce ecotropic cotran Viral supernatants were then used to infect differentiating cultures of stimulated murine CD8 T cells, as described [38,39]. Cells expressing F-tractin-EGFP were selected by at least 5 days of growth in EHAA media supplemented with IL-2 and 50 μg/mL Zeocin. The resulting selected populations of CD8 effector T cells were used for imaging experiments in the range of day 7 to day 12 following initiation of anti-TCR/anti-CD28 stimulation.

4.2. Preparation of stimulatory coverslips

8-well chambers (Cellvis, Mountain View, CA) were incubated with a 0.01% solution of poly-Llysine in distilled water for 10 minutes at room temperature. The dishes were there do a 37 \(\text{C} \) for 1 hour. Poly-L-lysine coated dishes were then incubated with 100 \(\text{Dg/m2} \) mouse anti-TCR\(\text{C} \) (clone H57-597, purified from hybridoma supernatant by protein G column enromatography) in 1X-PBS for either 1 hour at 37\(\text{D} \) cor overnight at 4\(\text{D} \) C. The coated chambers were then washed 5 times with Leibovitz's L-15 medium (Fisher Scientific).

4.3. Microscopy

T cells in L-15 medium without serum wate seeded on anti-TCR□ coated surfaces equilibrated to 37□C in a stage-top Okolab Incubator (Okolab S. R. L., Pozzuoli, NA, Italy). We chose to perform experiments without serum in order to obtain reproducible quantitative measurements. The large batch-to-batch variability in FBS could lead to experimental heterogeneity. In addition, serum can block antigen presentation to the T cells, affecting the extent to which plate-bound assays could activate the cells.

Interference reflection microscopy (IRM) and total internal reflection fluorescence (TIRF) images were acquired on an inverted Nikon Ti-E microscope (Nikon, Melville, NY), with 60X and 100X objectives (Nikon, Melville, NY) using a scientific CMOS camera (Andor, Concord, MA). IRM timelapse images were acquired every 3 seconds, while the TIRF images were acquired every 1 second.

4.4. Image Analysis

4.4.1. Area calculation from IRM images

In order to calculate the cell area from the IRM images, we first use the edge function with the Sobel operator in MATLAB® to detect a threshold based on the intensity gradients. We then tune the threshold value around this initial estimated threshold to obtain a bin representative of the contours of the cell. This binary image is then dilated and emoining holes are filled using the *imdilate* and *imfill* functions respectively in MATL nnected objects at the boundary are removed using the imclearborder function atasets with uneven backgrounds, this approach produced inconsistent segmentation n. In these cases, we used Trainable Weka Segmentation [42], a machine-learning based segmentation plugin in Fiji [43], in order to segment the IRM images. This approach was validated omparing the Weka segmentation with the MATLAB®-based segmentation on s with uniform illumination.

4.4.2. Edge dynamics

Cell boundaries were extracted units techniques detailed earlier [21]. Briefly, for each frame in the IRM stack, we first ow-pass filtered the image to remove shot noise and then corrected for non-uniform illumination. Histograms of the resulting pixel intensities typically exhibited a prominent peak corresponding to the background, a smaller peak corresponding to tightly adhered regions and a boad tail corresponding to the rest of the cell. Two thresholds were identified by visual inspection to mark the adhered and background pixels. An expectation-maximization algorithm using the thresholds as starting points was used to fit log-concave probability distributions to the background and dark pixels and mark the regions of the image as belonging to the background or the cell (dark and bright pixels, respectively). Dilation operations were used to

close the image and obtain a final binary image. An active contour algorithm [44] was applied to perform curvature-driven smoothing of the perimeter of the binary image and any selfintersections were removed. The thresholds were iteratively chosen by comparing computed cell areas in successive images in the time-lapse to minimize large changes. We then used a simplified version of the Machacek-Danuser algorithm [22] while maintaining the basic level set framew rk to ensure that the computed contours and edge velocities were topologically accurate. First, distance maps, which assign the distance of every grid point from successively sampled d ell contours at time t and t+dt were computed using the MATLAB® (Mathworks, ick, NA) function bwdist. A signed distance map was computed from the difference of o distance functions using the fast marching method [45]. A reinitialization procedure was rmed to ensure that the signed distance map remained a true distance function. The rest ting distance map is the normal distance nount that marker points on the contour at t need from the contour at time t to that at t+dt, i ontour. We ensured that the Frobenius norm r of the to be advected by in order to lie on the difference between the distance function computed from the advected marker points (the computed tour at t lay below a fixed threshold. As a cross-check, we contour at t+dt) and the original ution of the level set PDEs using a 4th order total variation diminishing verified that the direct 45] using a speed function computed above yielded similar results to our Runge-Kutta scheme simplified proc dure. The computed normal velocities along the contour were smoothed with a over 10 time points to produce the final velocity maps. The calculated edge indov velocities were down sampled by averaging along the arc length in blocks of 1 micron (sectors). This length-scale was chosen as it corresponded to the correlation length of the edge dynamics. The velocity time series of each sector was subjected to an empirical mode decomposition followed by a Hilbert-Huang transform in MATLAB® to obtain the instantaneous amplitude and instantaneous frequency distribution of each of the component modes. A maximum of 5 modes were calculated. The instantaneous amplitude values of the second and third modes were pooled across all sectors and all cells for each condition (WT or Bcl10^{-/-}) and compared using the Kolmogorov-Smirnov test.

4.4.3. Actin flow speeds

In order to quantify actin cytoskeletal dynamics, we used STICS to obtain sparotemptical velocity maps from the fluorescence images. STICS produces a matrix of velocity components, which we use to define a speed and a directional coherence (with respect to the control of the cell). The cumulative distribution function of speeds is constructed from speeds of each interrogation window in each time point of the phase. The data from all the cells is compiled into a cumulative distribution function. The probability density function of directional coherence is similarly defined as a normalized histogram of the individual directional coherences. We used a custom-made MATLAB® script to calculate the cumulative distribution function of the flow speeds from the velocity maps.

4.4.4. Directional cohered

The directional coherence for a region of interest (ROI) with flow velocity v_{ij} is defined as

$$\cos \theta_{ij} = \frac{v_{ij} \cdot r_{ij}}{v_{ij}}$$

where r_{ij} is the unit vector pointing from the ROI to the geometric centroid of the cell, and v_{ij} is the flow velocity for ROI (i,j). A directional coherence of +1 indicates a flow moving radially inward and a directional coherence of -1 indicates a flow moving radially outward.

We also defined a metric to quantify the spatial distribution of inward actin flows: the second spatial moment (SSM). We define a flow vector as being "inward" if the directional coherence is larger than 0.8. Once we identify the ROI's classified as having inward flow, the second spatial moment of the inward flows is defined as:

$$SSM = 2\sum_{i,j} r_{2ij} \cdot \cos \theta_{ij} \cdot H(\cos \theta_{ij} - 0.8) NR$$

Where N is the total number of ROI's with a directional coherence larger than 0.8, R is the maximum radius of the cell, r_{ij} is the distance of the ROI (i.) From the centroid, $\cos \theta_{ij}$ is the directional coherence, is the Heaviside function that is defined $x \in H$ $H(x-a) = \{0, x \le a \}$, $x \le a \}$

4.4.5. Identification of two temporal physes sing k-means clustering

We found that the results for the STICS analysis produced aberrant velocity maps for the first and last time point. In order to prevent uses outliers from biasing the clustering analysis, we first exclude these two time points from all analyses. We then use the *kmeans* function in MATLAB® to identify the optimal consters. Mathematically, the data could be represented by more than two clusters, but we restrict the number of states to two since we qualitatively observe only two distinct states: one was reasograde flow, and one with more disorganized flow. After the state assignment, we consider the time point whose state assignment differs from that of its two nearest (temporal) neighbors. These corrected points tend to lie at the interface of the two clusters, leading to an erroneous state assignment. This is the only user intervention in the process to identify the temporal phases.

Data Availability: All data supporting the findings of this study are available from the corresponding author upon reasonable request.

Acknowledgments

This work was supported by the National Institutes of Health (R01 GM131054 to x.O., U0) GM109887 and R01 AI125552 to B.C.S.). The authors thank Dr. T. Mak and he University Health Network (UHN), Toronto, CA for Bcl10^{-/-} mice.

Author Contributions

Kaustubh Wagh: Conceptualization, Methodology, Sftware, Formal analysis, Investigation,

Visualization, Writing-Original draft proparation. **Brittany Wheatley**: Investigation, WritingReview and Editing. **Maria Triver** Investigation, Writing-Review and Editing. **Imran Hussain**:

Investigation, Writing-Review and Aditing. Brian Schaefer: Conceptualization, Investigation, Writing-Review and Editing, Surery Sion, Funding Acquisition. Arpita Upadhyaya:

Conceptualization, Torkal Analysis, Visualization, Writing-Original draft preparation, Supervision, Project administration, Funding acquisition.

Reference

- [1] O. Acuto, D. Cantrell, T Cell Activation and the Cytoskeleton, Annu. Rev. Immunol. 18 (2000) 165–184. https://doi.org/10.1146/annurev.immunol.18.1.165.
- [2] M. Huse, The T-cell-receptor signaling network, J. Cell Sci. 122 (2009) 1269–1273. https://doi.org/10.1242/jcs.042762.

- [3] S. Etienne-Manneville, A. Hall, Rho GTPases in cell biology, Nature. 420 (2002) 629–635. https://doi.org/10.1038/nature01148.
- [4] L. Balagopalan, R.L. Kortum, N.P. Coussens, V.A. Barr, L.E. Samelson, The Linker for Activation of T Cells (LAT) Signaling Hub: From Signaling Complexes to Microclusters, J. Biol. Chem. 290 (2015) 26422–26429. https://doi.org/10.1074/jbc.R115.665869.
- [5] D.D. Billadeau, J.C. Nolz, T.S. Gomez, Regulation of T-cell activation by the cytoskeleton, Nat. Rev. Immunol. 7 (2007) 131–143. https://doi.org/10.1038/nri2021.
- [6] J.K. Burkhardt, E. Carrizosa, M.H. Shaffer, The Actin Cytoskeleton in T Cell Activation, Annu. Rev. Immunol. 26 (2008) 233–259. https://doi.org/10.1146/annurev.immunol.26.021607.090347.
- [7] P. Beemiller, M.F. Krummel, Mediation of T-cell activation by actin meskwasks, Cold Spring Harb. Perspect. Biol. 2 (2010) a002444. https://doi.org/10.1101/cshperspect.a002444.
- [8] K.L. Hui, L. Balagopalan, L.E. Samelson, A. Upadhyaya Cytosk letal forces during signaling activation in Jurkat T-cells, Mol. Biol. Cell. 26 (2011) 683–595. https://doi.org/10.1091/mbc.e14-03-0830.
- [9] K. Lam Hui, S.I. Kwak, A. Upadhyaya, Adhesion-dependent modulation of actin dynamics in Jurkat T cells, Cytoskelet. Hoboken NJ. 71 (2014) 119–123. https://doi.org/10.1002/cm.21156.
- [10] A. Babich, S. Li, R.S. O'Connor, M.C. Mildne B.D. Freedman, J.K. Burkhardt, F-actin polymerization and retrograde flow drive sestain d BLCγ1 signaling during T cell activation, J. Cell Biol. 197 (2012) 775–787. https://doi.org/10.1083/jcb.201201018.
- [11] S. Murugesan, J. Hong, J. Yi, D. Yi, J.P. Beach, L. Shao, J. Meinhardt, G. Madison, X. Wu, E. Betzig, J.A. Hammer, Formin generated actomyosin arcs propel T cell receptor microcluster movement at the immuse synapse, J. Cell Biol. 215 (2016) 383–399. https://doi.org/10.1083/jcb.201e03080.
- [12] A. Grakoui, S.K. Bromle, C. Lumen, M.M. Davis, A.S. Shaw, P.M. Allen, M.L. Dustin, The Immunological Synapse: A Molecular Machine Controlling T Cell Activation, Science. 285 (1999) 221–221. https://doi.org/10.1126/science.285.5425.221.
- [13] C.R.F. Monks, B.A. Freiberg, H. Kupfer, N. Sciaky, A. Kupfer, Three-dimensional segregation of su tramolecular activation clusters in T cells, Nature. 395 (1998) 82–86. https://doi.org/10.1038/25764.
- [14] M. Thome, V.E. Charton, C. Pelzer, S. Hailfinger, Antigen Receptor Signaling to NF-κB via CALMA, BCL10, and MALT1, Cold Spring Harb. Perspect. Biol. 2 (2010) a003004. https://doi.org/10.1101/cshperspect.a003004.
- [15] S. Full, B.C. Schaefer, A new look at T cell receptor signaling to nuclear factor-κB, Trends Impranol. 34 (2013) 269–281. https://doi.org/10.1016/j.it.2013.02.002.
- [16] T. Gehring, T. Seeholzer, D. Krappmann, BCL10 Bridging CARDs to Immune Activation, Front. Immunol. 9 (2018) 1539. https://doi.org/10.3389/fimmu.2018.01539.
- [17] J. Ruland, G.S. Duncan, A. Elia, I. del Barco Barrantes, L. Nguyen, S. Plyte, D.G. Millar, D. Bouchard, A. Wakeham, P.S. Ohashi, T.W. Mak, Bcl10 is a positive regulator of antigen receptor-induced activation of NF-kappaB and neural tube closure, Cell. 104 (2001) 33–42. https://doi.org/10.1016/s0092-8674(01)00189-1.

- [18] L.M. Kingeter, B.C. Schaefer, Loss of protein kinase C theta, Bcl10, or Malt1 selectively impairs proliferation and NF-kappa B activation in the CD4+ T cell subset, J. Immunol. Baltim. Md 1950. 181 (2008) 6244–6254. https://doi.org/10.4049/jimmunol.181.9.6244.
- [19] H.Y. Lu, B.M. Bauman, S. Arjunaraja, B. Dorjbal, J.D. Milner, A.L. Snow, S.E. Turvey, The CBM-opathies—A Rapidly Expanding Spectrum of Human Inborn Errors of Immunity Caused by Mutations in the CARD11-BCL10-MALT1 Complex, Front. Immunol. 9 (2018). https://doi.org/10.3389/fimmu.2018.02078.
- [20] D. Rueda, O. Gaide, L. Ho, E. Lewkowicz, F. Niedergang, S. Hailfinger, F. Rebeaud, M. Guzzardi, B. Conne, M. Thelen, J. Delon, U. Ferch, T.W. Mak, J. Ruland, M. Thomas Bcl10 Controls TCR- and FcγR-Induced Actin Polymerization, (n.d.) 13.
- [21] K. Lam Hui, C. Wang, B. Grooman, J. Wayt, A. Upadhyaya, Membrane Dwnan ics Correlate with Formation of Signaling Clusters during Cell Spreading, Biophys. J. 10. (2012) 1524–1533. https://doi.org/10.1016/j.bpj.2012.02.015.
- [22] M. Machacek, G. Danuser, Morphodynamic profiling of protrusion phenotypes, Biophys. J. 90 (2006) 1439–1452. https://doi.org/10.1529/biophysj.105.01033
- [23] X. Ma, O. Dagliyan, K.M. Hahn, G. Danuser, Profiling collular morphodynamics by spatiotemporal spectrum decomposition, PLoS Comput. Biol. 14 (2018) e1006321. https://doi.org/10.1371/journal.pcbi.1006321.
- [24] B.J. Belin, L.M. Goins, R.D. Mullins, Comparative arraysis of tools for live cell imaging of actin network architecture, BioArchitecture. 4 (2012) 189–202. https://doi.org/10.1080/19490992.2014.104.71
- [25] H.-G. Döbereiner, B.J. Dubin-Thale, J.M. Nofman, H.S. Xenias, T.N. Sims, G. Giannone, M.L. Dustin, C.H. Wiggins, M.P. Sheez, Laural membrane waves constitute a universal dynamic pattern of motile cells, Phys. Rev. Lett. 97 (2006) 038102. https://doi.org/10.1103/PhysRevLett.9.038102.
- [26] A.T. Ritter, S.M. Kapnick, S. Murugesan, P.L. Schwartzberg, G.M. Griffiths, J. LippincottSchwartz, Cortect actin recovery at the immunological synapse leads to termination of lytic granule secretion in cytotoxic T lymphocytes, Proc. Natl. Acad. Sci. U. S. A. 114 (2017) E6 65 E659 r. https://doi.org/10.1073/pnas.1710751114.
- [27] S. Kumari, D. Dep il, R. Martinelli, E. Judokusumo, G. Carmona, F.B. Gertler, L.C. Kam, C.V. Carman, & K. Burkhardt, D.J. Irvine, M.L. Dustin, Actin foci facilitate activation of the phospholipas C-vin primary T lymphocytes via the WASP pathway, ELife. 4 (2015). https://doi.org/10.7554/eLife.04953.
- [28] M. Fritzsch, P.A. Fernandes, V.T. Chang, H. Colin-York, M.P. Clausen, J.H. Felce, S. Gallani, C. Erlenkämper, A.M. Santos, J.M. Heddleston, I. Pedroza-Pacheco, D. Waithe, J.R. de la serna, B.C. Lagerholm, T.-L. Liu, T.-L. Chew, E. Betzig, S.J. Davis, C. Eggeling, Cytuskeletal actin dynamics shape a ramifying actin network underpinning immunological sympse formation, Sci. Adv. 3 (2017) e1603032. https://doi.org/10.1126/sciadv.1603032.
- [29] H. Colin-York, S. Kumari, L. Barbieri, L. Cords, M. Fritzsche, Distinct actin cytoskeleton behaviour in primary and immortalised T-cells, J. Cell Sci. 133 (2019). https://doi.org/10.1242/jcs.232322.
- [30] B. Hebert, S. Costantino, P.W. Wiseman, Spatiotemporal Image Correlation Spectroscopy (STICS) Theory, Verification, and Application to Protein Velocity Mapping in Living CHO Cells, Biophys. J. 88 (2005) 3601–3614. https://doi.org/10.1529/biophysj.104.054874.

- [31] S. Lloyd, Least squares quantization in PCM, IEEE Trans. Inf. Theory. 28 (1982) 129–137. https://doi.org/10.1109/TIT.1982.1056489.
- [32] J. Yi, X.S. Wu, T. Crites, J.A. Hammer, T.D. Pollard, Actin retrograde flow and actomyosin II arc contraction drive receptor cluster dynamics at the immunological synapse in Jurkat T cells, Mol. Biol. Cell. 23 (2012) 834–852. https://doi.org/10.1091/mbc.e11-08-0731.
- [33] I. Rey-Suarez, B.A. Wheatley, P. Koo, A. Bhanja, Z. Shu, S. Mochrie, W. Song, H. Shroff, A. Upadhyaya, WASP family proteins regulate the mobility of the B cell receptor during signaling activation, Nat. Commun. 11 (2020) 439. https://doi.org/10.1038/s41467-02014335-8.
- [34] O. Gaide, B. Favier, D.F. Legler, D. Bonnet, B. Brissoni, S. Valitutti, C. Fon, J. Tschopp, M. Thome, CARMA1 is a critical lipid raft–associated regulator of TCR-incided NF-κB activation, Nat. Immunol. 3 (2002) 836–843. https://doi.org/10.1038/ni.30.
- [35] B.C. Schaefer, J.W. Kappler, A. Kupfer, P. Marrack, Complex and dynamic r distribution of NF-κB signaling intermediates in response to T cell receptor stimulation. Proc. Natl. Acad. Sci. 101 (2004) 1004–1009. https://doi.org/10.1073/pnas.05.785.3100.
- [36] S. Marion, J. Mazzolini, F. Herit, P. Bourdoncle, N. Kambou-Lone, S. Hailfinger, M. Sachse, J. Ruland, A. Benmerah, A. Echard, M. Thome, F. Ni dergang, The NF-κB Signaling Protein Bcl10 Regulates Actin Dynamics by Controlling AP1 and OCRL-Bearing Vesicles, Dev. Cell. 23 (2012) 954–967. https://doi.org/10.1016/j.devcel.2012.09.021.
- [37] F. Tamzalit, M.S. Wang, W. Jin, M. Tello-La oz M. Boyko, J.M. Heddleston, C.T. Black, L.C. Kam, M. Huse, Interfacial actin protruction mechanically enhance killing by cytotoxic T cells, Sci. Immunol. 4 (2019). http://loi.org/10.1126/sciimmunol.aav5445.
- [38] M.K. Traver, S. Paul, B.C. Schaefer, T Cell Receptor Activation of NF-κB in Effector T Cells: Visualizing Signaling Event Within and Beyond the Cytoplasmic Domain of the Immunological Synapse, Methods Mol. Biol. Clifton NJ. 1584 (2017) 101–127. https://doi.org/10.1007/978-1-939-6881-7 8.
- [39] S. Paul, B.C. Schaefer, A calling TCR-induced POLKADOTS formation and NF-κB activation in the D10 T-cell close and mouse primary effector T cells, Methods Mol. Biol. Clifton NJ. 1280 (2715, 21, 238. https://doi.org/10.1007/978-1-4939-2422-6 12.
- [40] B.C. Schaefer, AD. Stronlinger, S.H. Speck, Redefining the Epstein-Barr virus-encoded nuclear antigen EBNA 1 gene promoter and transcription initiation site in group I Burkitt lymphoma celllines, Proc. Natl. Acad. Sci. U. S. A. 92 (1995) 10565–10569. https://doi.org/10.1073/pnas.92.23.10565.
- [41] R.K. variaus, L. Costanzi, M. Haas, I.M. Verma, The pCL vector system: rapid production of h lper-1 ee, high-titer, recombinant retroviruses, J. Virol. 70 (1996) 5701–5705.
- [42] I. Arganea-Carreras, V. Kaynig, C. Rueden, K.W. Eliceiri, J. Schindelin, A. Cardona, H. Sebastian Seung, Trainable Weka Segmentation: a machine learning tool for microscopy place classification, Bioinformatics. 33 (2017) 2424–2426. https://doi.org/10.1093/bioinformatics/btx180.
- [43] J. Schindelin, I. Arganda-Carreras, E. Frise, V. Kaynig, M. Longair, T. Pietzsch, S. Preibisch, C. Rueden, S. Saalfeld, B. Schmid, J.-Y. Tinevez, D.J. White, V. Hartenstein, K. Eliceiri, P. Tomancak, A. Cardona, Fiji: an open-source platform for biological-image analysis, Nat. Methods. 9 (2012) 676–682. https://doi.org/10.1038/nmeth.2019.

- [44] Chenyang Xu, J.L. Prince, Gradient vector flow: a new external force for snakes, in: Proc. IEEE Comput. Soc. Conf. Comput. Vis. Pattern Recognit., IEEE Comput. Soc, San Juan, Puerto Rico, 1997: pp. 66–71. https://doi.org/10.1109/CVPR.1997.609299.
- [45] S. Osher, R. Fedkiw, Level set methods and dynamic implicit surfaces, Springer, New York, 2003.

,00,5

Figure Captions

Figure 1: Spreading and morphological dynamics of act T cells. (a) Time lapse of interference reflection microscopy (IRM) images of X-1, top panels) and Bcl10^{-/-} (bottom panels) primary mouse effector T cell spreading on st ula bry coverslip coated with anti-TCRB antibody. Scale bar: 5 μm. (b) Representative spreading curves for WT (black) and Bcl10^{-/-} (red) cells. Datapoints are marked as dots, and the smooth curves are the tanh fits. (c) Spreading rates of WT (N = 34) and Bc110 $^{-/-}$ (N 35) cells. K-S test shows that the variances are significantly hrs a a function of time for WT (left panels) and Bcl10^{-/-} (right different (P < 0.05). (d) Cell con panels). Contour color scheme scale from blue to red with blue contours representing early times and red representing late times. Contours are plotted between 7-11 min after spreading initiation, when the call had maximally spread. Scale bar: 5 µm. (e) Heat maps of edge velocities calculated from contrars in (d) using a level-set algorithm. The colors correspond to the velocity the color bar. The two left panels are for WT cells and the two right panels values as. cells. Protrusions are in red and retractions are in blue. (f)-(g) Cumulative distribution function of the amplitude of Modes 2 and 3 respectively from the empirical mode decomposition of edge velocities (calculated between 4 and 11 minutes of spreading) for a population of WT (black, N=7) and Bcl10^{-/-} (red, N=9) cells. K-S test shows that the distributions are significantly different ($P < 10^{-5}$).

Figure 2: Analysis of actin dynamics reveals qualitative temporal differences in actin flows (a) Time lapse TIRF images of F-tractin-EGFP labeled spreading T cells (top panels: WT cells, bottom panels: Bcl10^{-/-} cells) showing the clearance of actin in the central region following subsequent recovery of actin in the entire contact zone. (b) Time lapse montage of a WT CD8 primary mouse effector T cell expressing F-tractin-EGFP spreading on a stimulatory glass coverslip coated with anti-TCRβ antibody. Scale bar: 5 μm. (c) Spatiotemporal image correlation spectroscopy (STICS) analysis illustrating the spatiotemporal behavior of actia was at the immune synapse. Yellow arrows corresponding to velocity vectors over a region of interest are superimposed on a TIRF snapshot (left panel). The lower panel shows a zammed in view of the area enclosed by the red box. (d) Spatial heat map showing the magnitudes of actin flows speeds at three time points. Colors correspond to the speed as indicated in the celler bar. (e) Spatial heat map showing the directional coherence of actin flows at three time points. Colormap is on a scale such that blue indicates flows away from the center and yellow advertes flows towards the center.

Figure 3: Temporal dynamics of active flo turing T cell activation. (a)-(e) Panels show results for one representative cell (a) Probability density functions of speeds obtained from STICS plotted for several sampletimes. Blue indicate early times and yellows indicate later times. (b) Scatter plot of mean and standard leviation of the distributions of speeds. Blues indicate early times and yellows indicate later times. (c) Results of k-means clustering into two clusters. (d) , color-coded according to the clusters identified in (c). Shaded Mean speed as a function of ime error bars indicate 25/6*s indard error. (e) The second spatial moment (SSM) of inward flows of the same cell as in (a)-(1) plotted as a function of time. The SSM is used to quantify the spatial distribution of h war I flows (i.e. directional coherence > 0.8). (f) The cumulative distribution function of actin flow speeds obtained from STICS analysis for WT cells (N = 12 cells). Flow Phase 1 (blue line) are higher than those in Phase 2 (orange lines), as indicated by a speeds N whift in the CDF for Phase 2. These distributions are significantly different (p<10⁻⁵³, Kolmogorov-Smirnov test). (g) The probability density function of directional coherence obtained from STICS analysis for WT cells (Phase 1 in blue, and Phase 2 in orange). Inset shows that flows in Phase 1 (blue) display a higher probability of inward (retrograde) flow than those in Phase 2

(blue). (p < 3E-6, proportions test). (h) Boxplot of second spatial moment (SSM) of inward flow for Phase 1 (blue) and Phase 2 (orange) (***p<10⁻⁷¹, Mann-Whitney U test, N = 12 cells).

Figure 4: Bcl10^{-/-} cells display higher actin flow speeds compared to WT cells (a) Time lapse images of a Bc110^{-/-} primary mouse effector T cell expressing F-tractin-EGFP spreading on a stimulatory glass coverslip coated with anti-TCRB antibody. Scale bar: 5 un (b) T montage of heatmaps of flow speeds obtained from STICS analysis at three time points for a representative Bcl10^{-/-} cell. The colors correspond to speeds as indicated in the colorbar. (c) Time lapse montage of heatmaps of directional coherence from STICS anal sis a the same three time points for the same cells. The colors correspond to inward (yellow) and antward (blue) flows. (d) Comparison of cumulative distribution function of actin flow speets in WT (solid lines) and Bc110-/- (dashed lines) cells, with Phase 1 flows in blue and Phase 2 flows in orange. ($p < 10^{-27}$, Kolmogorov-Smirnov test, N=12 WT and N=21 Bollows. (e) Probability density of directional coherence for WT (solid lines) and Bcl10^{-/-} (das red lines) cells shows no significant difference. Within each condition, the proportion of inward how is higher in Phase 1 (blue) than in Phase 2 (orange) (p<10⁻⁵, proportions test). (f) Box tots of second spatial moment of inward flow for WT and Bc110-KO in the two different chases (Phase 1 in blue, Phase 2 in orange) (*** p<10⁻⁷² Mann Whitney U Test). (g)-(h) Currentive distribution functions for the second spatial moment of inward flows plotted for Phase 1 (g) and Phase 2 (h). Black lines represent quantification for WT cells, while red lines represent that for Bcl10^{-/-} cells. Solid lines indicate the empirical CDF, while the dotted lines indica e the 99% confidence intervals.

Author Contributions

Kauktub Wag h: Conceptualization, Methodology, Software, Formal analysis, Investigation, Visualization, Writing-Original draft preparation. Brittany Wheatley: Investigation, WritingReview and Editing. Maria Traver: Investigation, Writing-Review and Editing. Imran Hussain:

Investigation, Writing-Review and Editing. **Brian Schaefer**: Conceptualization, Investigation, Writing-Review and Editing, Supervision, Funding Acquisition. **Arpita Upadhyaya**: Conceptualization, Formal Analysis, Visualization, Writing-Original draft preparation, Supervision, Project administration, Funding acquisition.

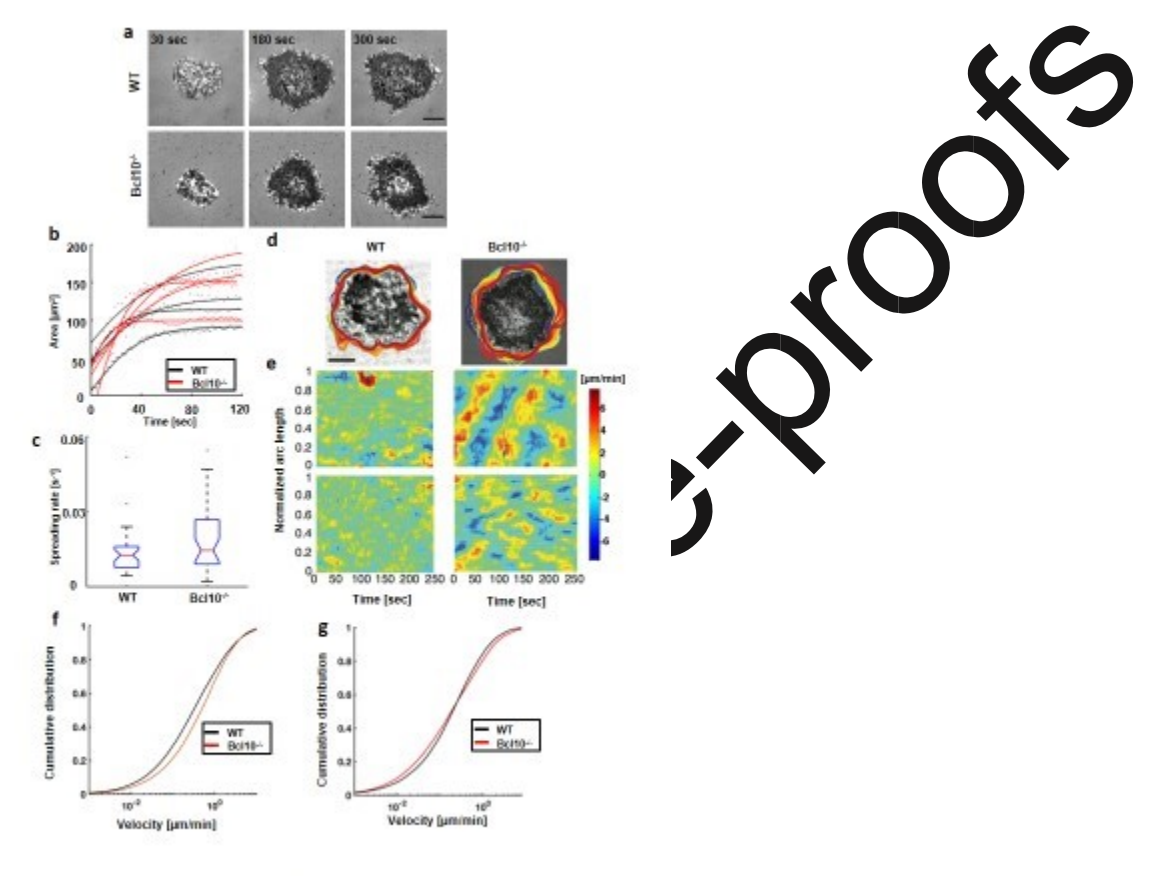


Figure 1



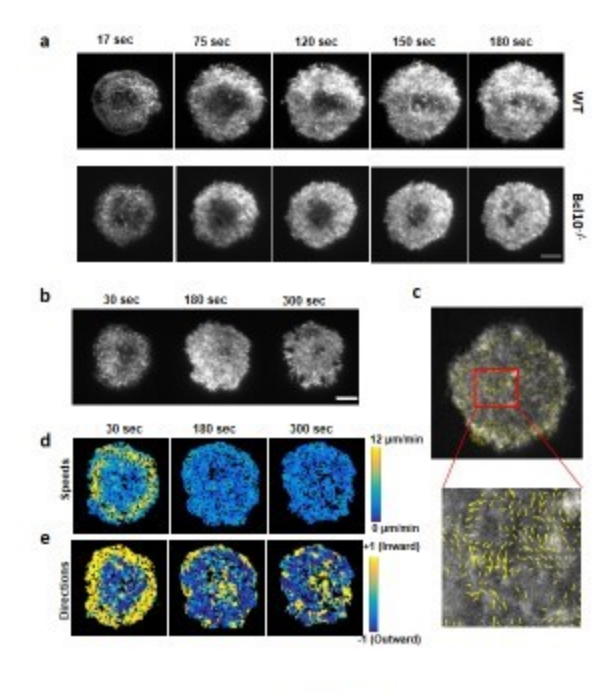
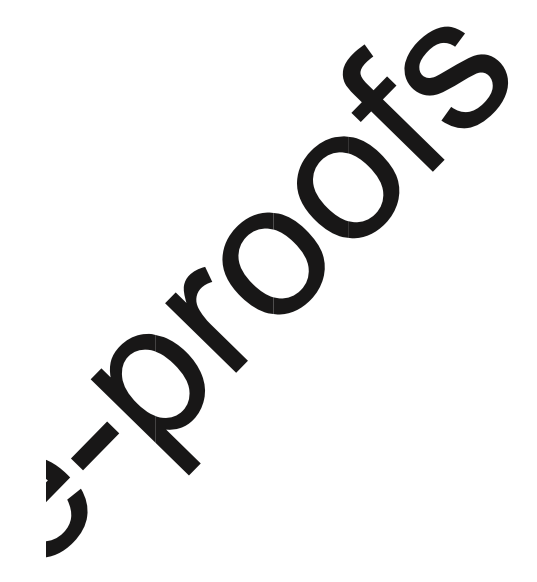
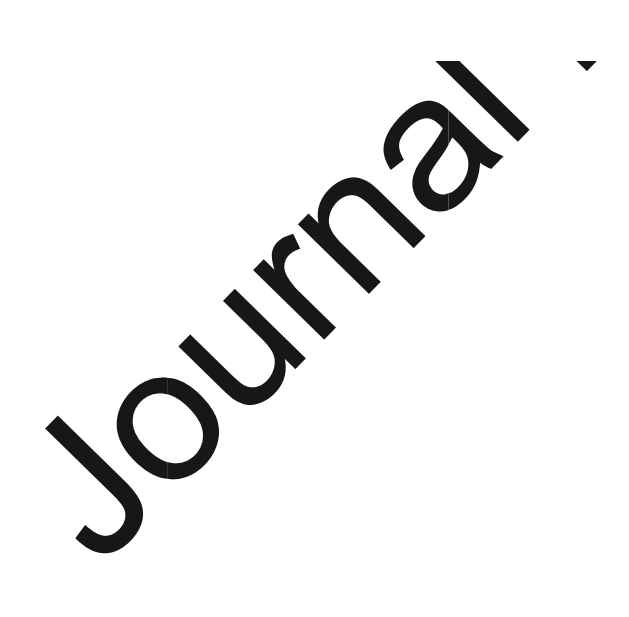
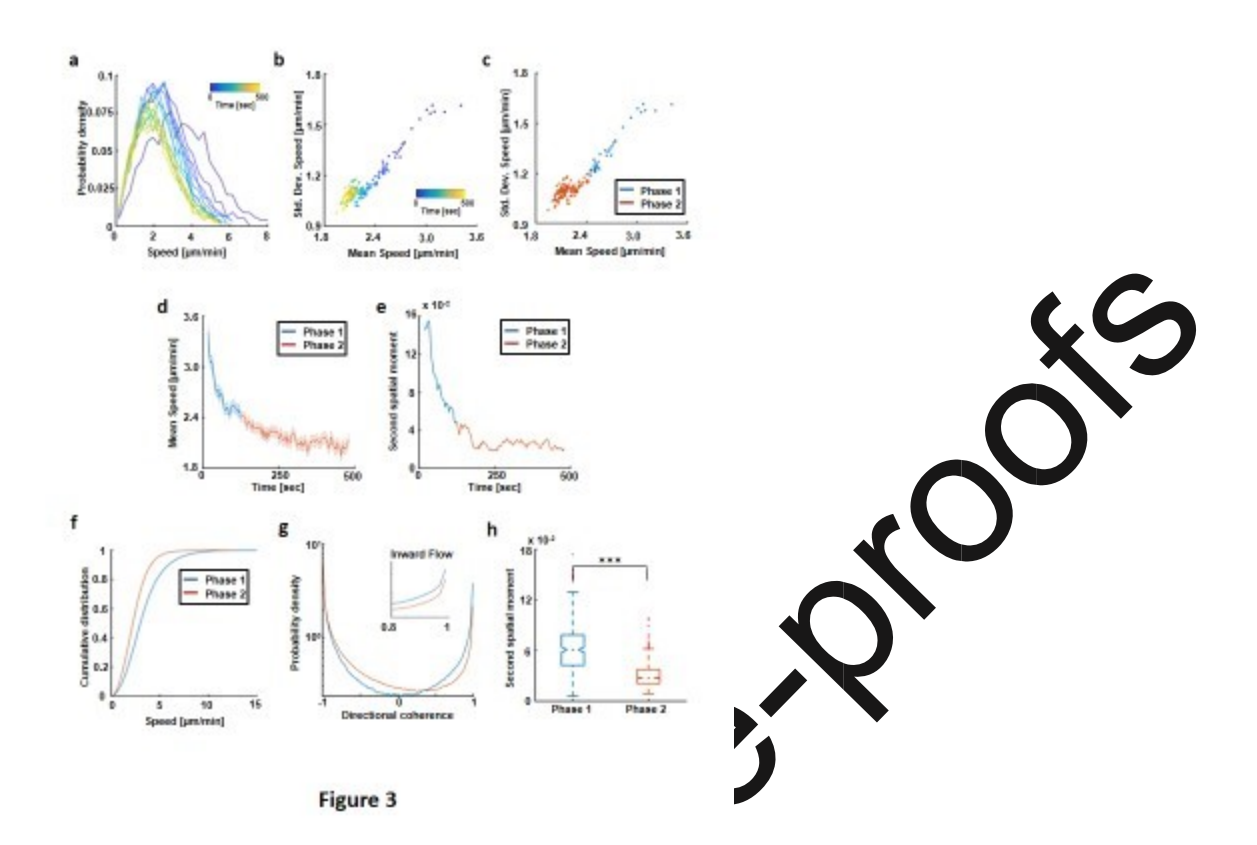


Figure 2









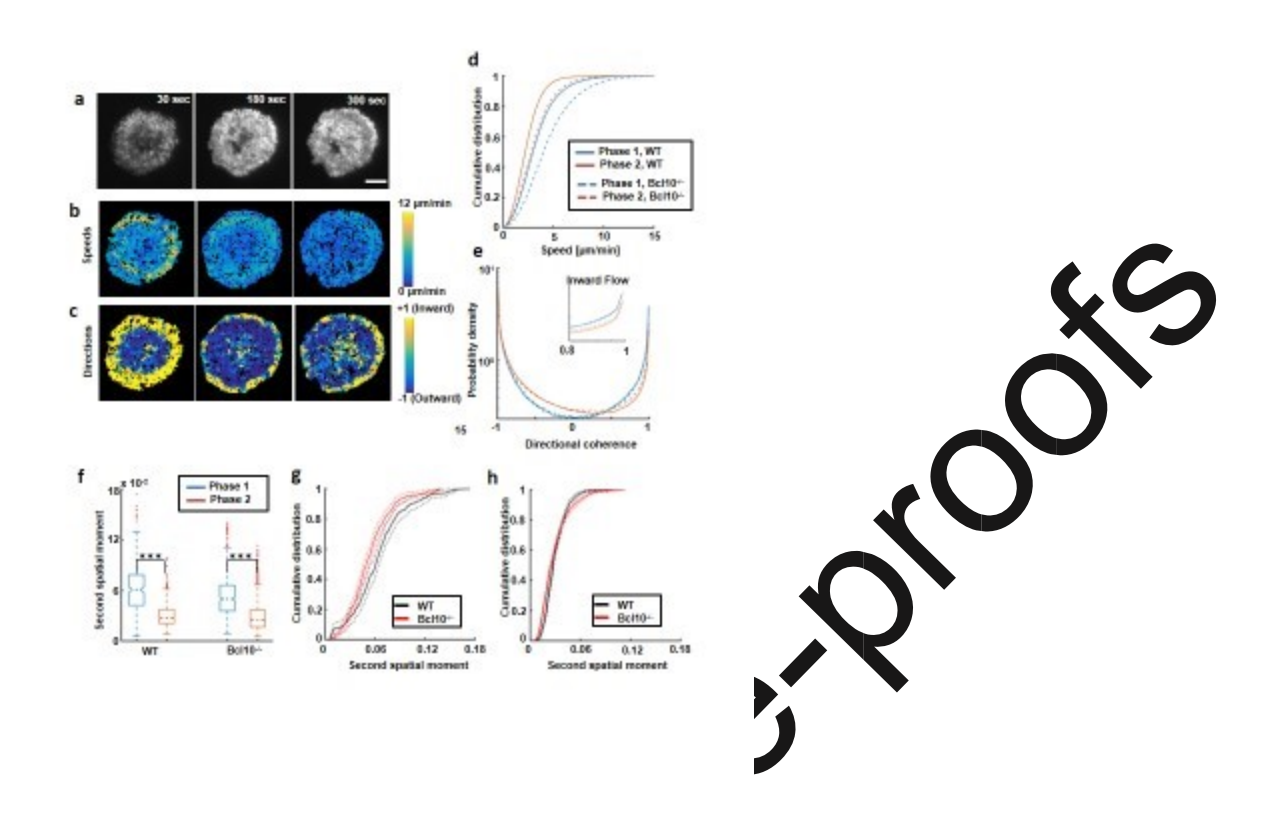


Figure 4

Highlights for Wagh et al. "Bcl10 is associated with actin dynamics at the T cell immune synapse"

- ▲ A tin dynamics in TCR-activated primary CD8 effector T cells show two phases
- Bcho gulates lamellipodial dynamics in activated effector T cells
- T ells lacking Bcl10 display faster actin flow speeds upon TCR stimulation
- Study indicates an NF-DB-independent role for Bcl10 in early TCR mediated signaling